fluids

MDPI

Article

Numerical Study on the Impact Pressure of Droplets on Wind Turbine Blades Using a Whirling Arm Rain Erosion Tester

Nobuyuki Fujisawa [1,*] and Hirokazu Kawabata [2]

[1] Faculty of Engineering, Shinshu University, 4-17-1 Wakasato, Nagano 380-8553, Nagano, Japan
[2] Renewable Energy Research Center, National Institute of Advanced Industrial Science and Technology, 2-2-9 Machiikedai, Koriyama 963-0298, Fukushima, Japan; kawabata-h@aist.go.jp
* Correspondence: fujisawa@eng.niigata-u.ac.jp

Abstract: The leading-edge erosion of a wind turbine blade was tested using a whirling arm rain erosion tester, whose rotation rate is considerably higher than that of a full-scale wind turbine owing to the scale effect. In this study, we assessed the impact pressure of droplets on a wet surface of wind turbine blades using numerical simulation of liquid droplet impact by solving the Navier–Stokes equations combined with the volume-of-fluid method. This was conducted in combination with an estimation of liquid film thickness on the rotating blade using an approximate solution of Navier–Stokes equations considering the centrifugal and Coriolis forces. Our study revealed that the impact pressure on the rain erosion tester exceeded that on the wind turbine blade, attributed to the thinner liquid film on the rain erosion tester than on the wind turbine blade caused by the influence of centrifugal and Coriolis forces. This indicates the importance of correcting the influence of liquid-film thickness in estimating the impact velocity of droplets on the wind turbine blade. Furthermore, we demonstrated the correction procedure when estimating the impact velocity of droplets on the wind turbine blade.

Keywords: liquid droplet impact; erosion tester; impact pressure; liquid film; wind turbine blade

check for updates

Citation: Fujisawa, N.; Kawabata, H. Numerical Study on the Impact Pressure of Droplets on Wind Turbine Blades Using a Whirling Arm Rain Erosion Tester. *Fluids* **2024**, *9*, 160. https://doi.org/10.3390/fluids9070160

Academic Editor: Sergey Smolentsev

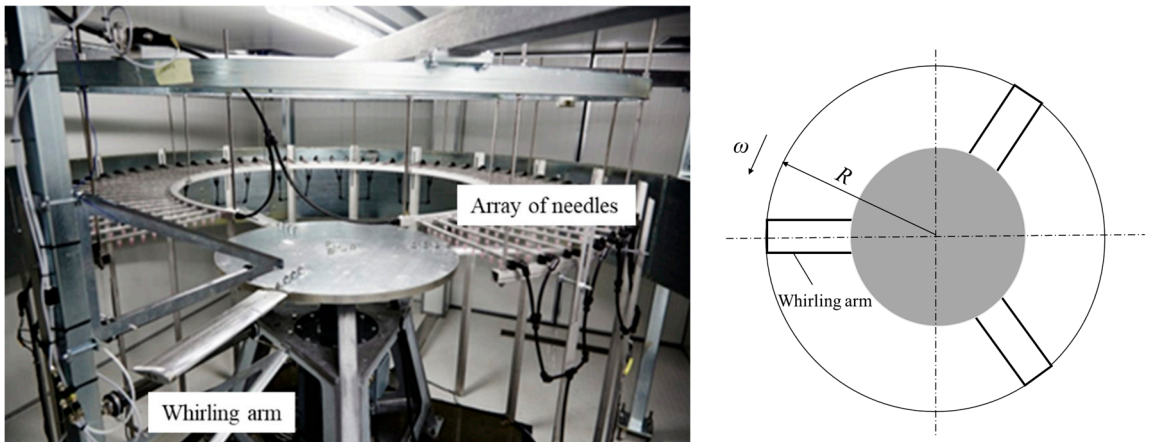
Received: 7 May 2024
Revised: 12 July 2024
Accepted: 13 July 2024
Published: 15 July 2024

Copyright: © 2024 by the authors. Licensee MDPI, Basel, Switzerland. This article is an open access article distributed under the terms and conditions of the Creative Commons Attribution (CC BY) license (https://creativecommons.org/licenses/by/4.0/).

1. Introduction

Liquid droplet impingement erosion has been a fundamental topic of interest in engineering for many years [1–3]. This topic has been investigated in regard to the engineering problem of material erosion that occurs in liquid droplet impingement on gas and steam turbine blades [4,5], wall thinning of carbon-steel pipelines in nuclear/fossil power plants [6,7], rain erosion on flying aircraft [8], and leading-edge erosion of wind turbine blades [9–16]. However, the erosion mechanisms are not fully understood owing to the complexity of the erosion phenomenon caused by the highly different droplet sizes of steam (10 μm in diameter) and rain (a few millimeters in diameter), as well as their impact velocity ranges from low (approximately 10 m/s) to high (up to 1000 m/s), which is observed in aircraft applications [8]. Furthermore, the influence of the liquid film on the initiation of erosion presents a challenging problem, as it can significantly alter the peak impact pressure of the droplet on the wall materials [3,16].

To study the rain erosion behavior of wind turbine blades, a whirling arm rain erosion tester (see Figure 1) has become the de facto standard for testing the initiation of erosion on a wind turbine blade [17–20]. During the operation of the whirling arm erosion tester, numerous droplets with diameters of a few millimeters fall from needles to simulate rainfall on a rotating wind turbine blade. In general, the blade radius of the rain erosion tester typically ranges from 0.5 to 1.5 m, which is one or two orders of magnitude lower than that of the wind turbine blade, from 20 to 100 m. Consequently, the wet blade in the rain erosion tester experiences a much higher rotation rate, resulting in the increase in centrifugal and Coriolis forces compared with those in the wind turbine, to maintain the same impact velocity of the droplet, which is the main component of blade erosion.



(**a**) Image of whirling arm rain erosion tester (**b**) Top view

Figure 1. Whirling arm rain erosion tester for the wind turbine blade [19].

When liquid droplets collide with a wind turbine blade under rainy conditions, they form a liquid film on the wall. The thickness of the film increases with an increase in the number of impacts and is highly influenced by the centrifugal and Coriolis forces on the rotating blade [16]. Thus, the thickness of the liquid film on the blade may vary depending on the rotation rate, blade radius, and rainfall rate. However, in previous studies [8], the influence of a liquid film has not been considered, as the liquid film may be sufficiently thin in high-speed flow applications. However, this influence may not be negligible in low-speed flow applications such as wind turbine blades.

The influence of a liquid film on the erosion of material by droplet impact was first noticed by Brunton and Rochester [21], who suggested that the divergence of a pressure wave passing through the liquid film may reduce the impact pressure of the droplet on the wet wall. This was similarly argued in the development of pulsed-jet rain erosion testers [22,23]. More recently, the influence of a liquid film on erosion was experimentally investigated during droplet impact at velocities of 118–168 m/s [24,25] in a laboratory test, which is the velocity range of wind turbine blades. The results show that the erosion rate decreased owing to an increase in the liquid-film thickness, thus demonstrating the reduction in the impact pressure of the droplet owing to the liquid film.

The fluid dynamics of liquid droplets impacting dry and wet walls were numerically investigated, with an emphasis on high-speed droplet impacts. Haller et al. [26] investigated high-speed droplet impacts numerically for a droplet of 200 μm in diameter impacting drywall at a velocity of 500 m/s. They observed shockwave creation inside the droplet, propagation in the droplet, and interaction with the free surface, which resulted in the formation of a high-speed lateral jet reaching a maximum velocity of 6000 m/s. Subsequently, the high-speed impact of a 50 μm droplet on a wet wall was numerically investigated [27]. The results showed that the impact pressure of the droplet on a wet wall was smaller than that on a drywall, thus suggesting a damping effect on the impact pressure of the droplet owing to the liquid film. Further numerical studies considering material properties [28,29] showed that the variation in the equivalent stress inside a material caused by the impact pressure on a wet wall was significantly lower than that on a drywall. Moreover, numerical and experimental studies pertaining to droplet impact on rough surfaces with and without liquid films have been conducted [30–32]. The results showed that erosion on a rough surface was caused by erosion initiation near the groove trough, followed by the removal of the groove peak roughness. These studies show that liquid films significantly affect impact pressure and thus should not be disregarded in low-speed flow applications; however, the influence of liquid films has not been considered in the field of wind turbines.

In this study, we aimed to numerically investigate the impact pressure damping effect of a rain droplet on a rotating blade by numerically solving the Navier–Stokes equations combined with the volume-of-fluid method, where the liquid film thickness on the wall was determined by the approximate solutions of Navier–Stokes equations. The computations were conducted for the conditions of the rain erosion tester and wind turbine blades of wet walls. Furthermore, the correction procedure of impact velocity on the wind turbine blade was subsequently presented using the test results of a whirling arm rain erosion tester.

2. Numerical Methods

2.1. Numerical Simulation of Droplet Impact

Numerical simulations of droplet impact on a wet wall were performed by solving the unsteady axisymmetric Navier–Stokes Equation (1) with the continuity Equation (2), which are written as follows:

$$\frac{\partial \boldsymbol{V}}{\partial t} + \nabla \cdot (\boldsymbol{VV}) = -\frac{1}{\rho}\nabla p + \frac{\mu}{\rho}\nabla^2 \boldsymbol{V} + \frac{1}{\rho}\boldsymbol{F} \tag{1}$$

$$\nabla \cdot \boldsymbol{V} = 0, \tag{2}$$

where $\boldsymbol{V}$ is the velocity vector; p is the pressure; t is the time; μ is the fluid viscosity; ρ is the fluid density; and $\boldsymbol{F}$ represents the external forces exerting on the fluid, such as the gravitational acceleration and surface tension.

These governing equations were solved numerically using the volume-of-fluid method to evaluate the peak pressure of a droplet impacting a wet wall. The model included a linear volume-tracking algorithm to track the deformation of the free surface. The interface is defined by a scalar function f representing the fraction of the volume of a cell that contains a liquid, which is equal to 1 if the cell is full, 0 if it is empty, and between 0 and 1 if the cell contains a free surface. The scalar function f is passively advected by the flow and can be expressed as follows:

$$\frac{\partial f}{\partial t} + (V \cdot \nabla) f = 0 \tag{3}$$

A numerical simulation was conducted using the commercial software FLUENT to analyze the behavior of the impact of spherical liquid droplet with a diameter of 3 mm on a wet wall, as shown in Figure 2. We assumed that the liquid film had a uniform thickness on the wall and the impact behavior of the spherical droplet was incompressible as the Mach number was small [33].

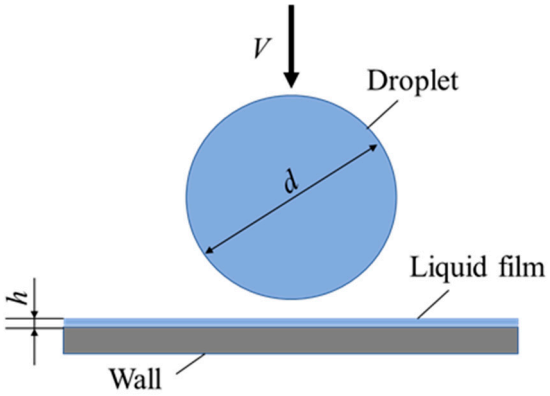


Figure 2. Illustration of a droplet impact model on a wet wall.

To numerically solve the unsteady axisymmetric Navier–Stokes equations combined with the continuity equation, the governing equations were discretized using the second-order upwind scheme. The pressure-velocity calculations were conducted using the pressure implicit with splitting of the operator (PISO) algorism. The time step was set to

1×10^{-6} s with 20 internal iterations in each time step. The numerical simulation was considered convergent when the residuals decreased below 1×10^{-5}. The non-slip boundary condition was applied to the wall and the zero-gradient condition was set on the surrounding free boundaries, whereas the axisymmetric boundary condition was applied along the center of the liquid droplet. In the numerical simulation, the computational domain was set to 30 mm × 20 mm in the radial and vertical directions, respectively. The calculations were conducted with 260 grids across the droplet. The orthogonal computational grids were adopted, as shown in Figure 3. The grid independence tests showed that the peak pressure coefficient at the droplet center was $C_{pc} = 4.2 \pm 0.2$, which was unaffected by the number of grids across the droplet in the range of 200 to 260 grids. This suggested that the peak central pressure coefficient was insensitive to the current grid resolutions for analyzing the droplet impact on a wet wall ($h/d = 0.1$). Notably, this grid resolution of 260 across the droplet is reasonable, as indicated by a previous study [33], as the central peak pressure is insensitive to the droplet impact on drywall. Furthermore, the computational analysis of the impact force on dry and wet walls during low-speed droplet impact at a velocity of $V = 4.6$ m/s was in agreement with the force-sensor measurement within an experimental uncertainty of measurement [34]. This confirms the validation of the current computation.

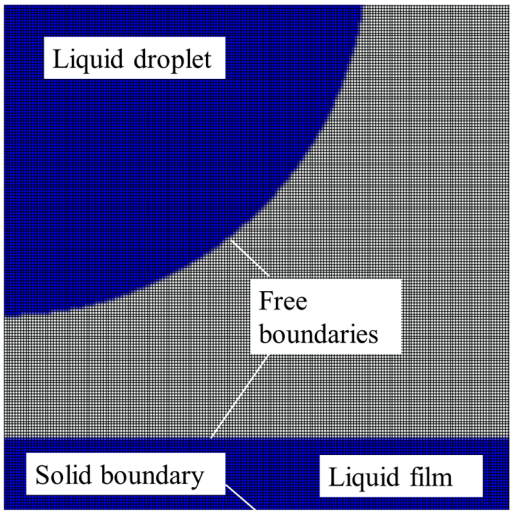


Figure 3. Example of computational grids of droplet impact on a wet wall.

The calculations were conducted by releasing a droplet near the wet wall at a height of 0.05 d, with a specified droplet impact velocity V perpendicular to the wall. The droplet diameter was assumed to be 3 mm. This relatively large droplet diameter of rain was considered in the calculation, as the erosion volume in unit time increases in proportion to the third power of the droplet diameter [29]. This suggests that the relatively larger droplets may have a significant influence on the initiation of erosion. The impact pressure on the wet wall was calculated for various combinations of radial positions from the center of rotation, impact velocities, and rainfall rates. The results were then compared with those of the drywall counterpart with a zero liquid-film thickness on the wall.

2.2. Estimation of Liquid-Film Thickness

To predict the impact pressure on a rotating wet wall during rain, the thickness of the liquid film on the wind turbine blade must be assessed, as it highly influences the peak pressure of rain droplets impacting the blade. In this study, the liquid-film thickness on the rotating blade was assessed by applying the approximate solution of Navier–Stokes equations for axisymmetric liquid-film flow over a rotating wall with a non-slip boundary condition on the rotating disk and zero-gradient condition on the free surface. Notably, the effects of centrifugal and Coriolis forces were considered in the analysis. In this approximate solution, the influence of inertial forces, gravity, surface tension, and frictional forces

of airflow was assumed to be negligible compared with that of the centrifugal and Coriolis forces in the liquid film on the wall [35]. We did not address the impact of droplets on a curved wall owing to the complexity of the analysis [36]. These assumptions were made to estimate the thickness of the liquid film; as in this study, we primarily focused on the effects of centrifugal and Coriolis forces. This approach provides a starting point for estimating the behavior of the liquid film on wind turbine blades. Further detailed studies that evaluate the local liquid-film thickness on wind turbine blades should be conducted in the future.

Under these considerations, the liquid film thickness h on the rotating blade was determined by considering the centrifugal and Coriolis forces. This was achieved by assuming that the rainfall was uniform over the rotating blade with a rainfall rate I (in mm per hour) and that the liquid velocity normal to the wall was smaller than that in the radial direction. The liquid film thickness, h, can be approximated by the following equation [35];

$$h = 0.886\, Q^{0.348}\, \nu^{0.328}\, \omega^{-0.676}\, R^{-0.70} \tag{4}$$

with

$$Q = 8.72 \times 10^{-7} R^2\, I \tag{5}$$

where Q (m^3/s) represents the rain flow rate on the rotating disk, R is the radius of the rotating blade (m), ν is the kinematic viscosity of water (m^2/s), and ω is the angular velocity (rad/s). Notably, the impact velocity V of the droplet can be obtained from $R\omega$.

3. Results and Discussion

3.1. Droplet Impact Behavior on a Wet Wall

Figure 4 shows the time variation in the droplet contours impacting the dry (h/d = 0) and wet walls (h/d = 0.1) at an impact velocity of V = 100 m/s with a typical droplet diameter of d = 3 mm. The behavior of a droplet impacting a drywall demonstrates the lateral spreading of the droplet after impact. In contrast, when a droplet impacts a wet wall, it immediately splashes after generating lateral jets. This can be attributed to the influence of the reflected impact pressure in the liquid film. Although the splash initially developed in the lateral direction (tV/d = 0.1), it shifted to a vertical direction owing to the influence of the lateral jet spreading along the wall (tV/d = 0.2–0.6). Notably, the maximum lateral jet velocity on the drywall was 8.7-fold the impact velocity V, whereas it was 9.2 on the wet wall. The higher lateral jet velocity on the wet wall can be attributed to the slip condition on the free surface of the liquid film, whereas the non-slip existed on the solid wall.

Figure 5 shows the time variation in the contours of the pressure coefficient C_p of a droplet impacting the dry and wet walls (h/d = 0.1), obtained at an impact velocity of V = 100 m/s with a droplet diameter of d = 3 mm. The pressure coefficient is defined as $C_p = (p - p_s)/(\frac{1}{2}\rho V^2)$, where p is the pressure, p_s is the surrounding pressure, and ρ is the density of fluid). Although the peak impact pressure occurred immediately after the droplet impacted the drywall at the contact edges of the droplet impact (tV/d = 0.01), the peak pressure coefficient on the wet wall decreased at the center owing to the impact pressure damping effect of the liquid film on the wet wall. After the droplet impacted the wet wall, the peak impact pressure on the wet wall decreased and the splash formation occurred on the liquid film (tV/d = 0.1). The peak impact pressure subsequently tended to increase and the lateral extent of the high-pressure region expanded over the wet wall (tV/d = 0.2). The pressure contour extended laterally to the location of the splash, indicating an increased impact pressure area caused by the formation of the splash on the wet wall (tV/d = 0.4). The lateral jet then continued to spread out in a radial direction (tV/d = 0.6) and the impact pressure increased slightly compared with that on the drywall. This suggests that the impact force increased in the latter stage of droplet impact on the wet wall, as observed under a very low droplet impact condition (impact velocity lower than 10 m/s) on a wet wall [34,37]. Notably, the impact force behavior on a wet wall at high velocity (V = 100 m/s) is very similar to that at low velocity (V = 4.6 m/s).

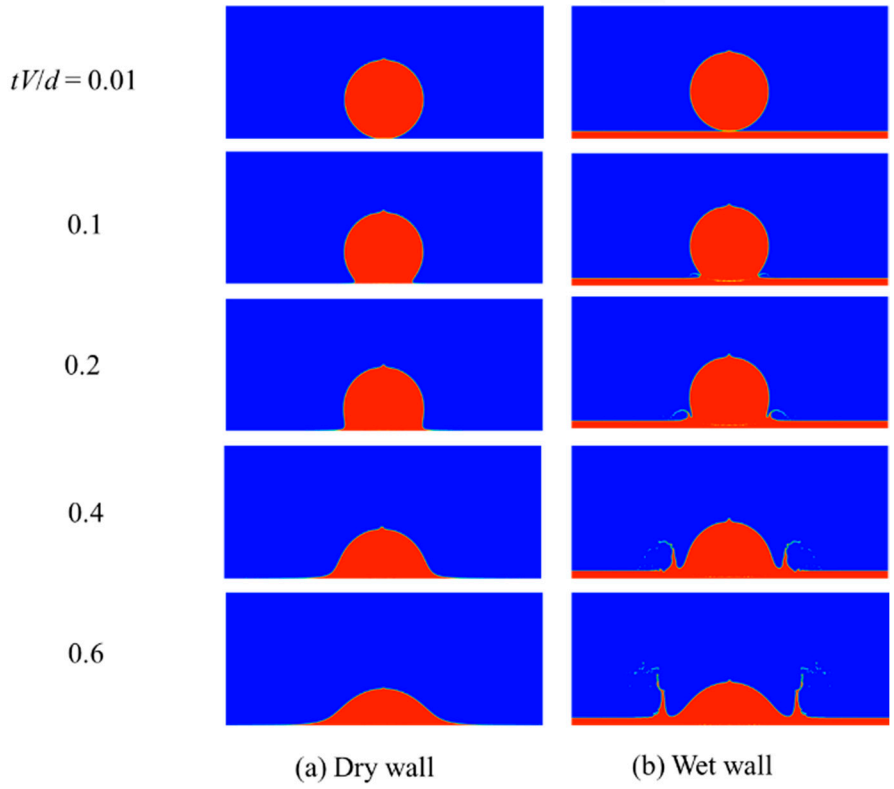


Figure 4. Time variation in droplet contours during droplet impact (V = 100 m/s).

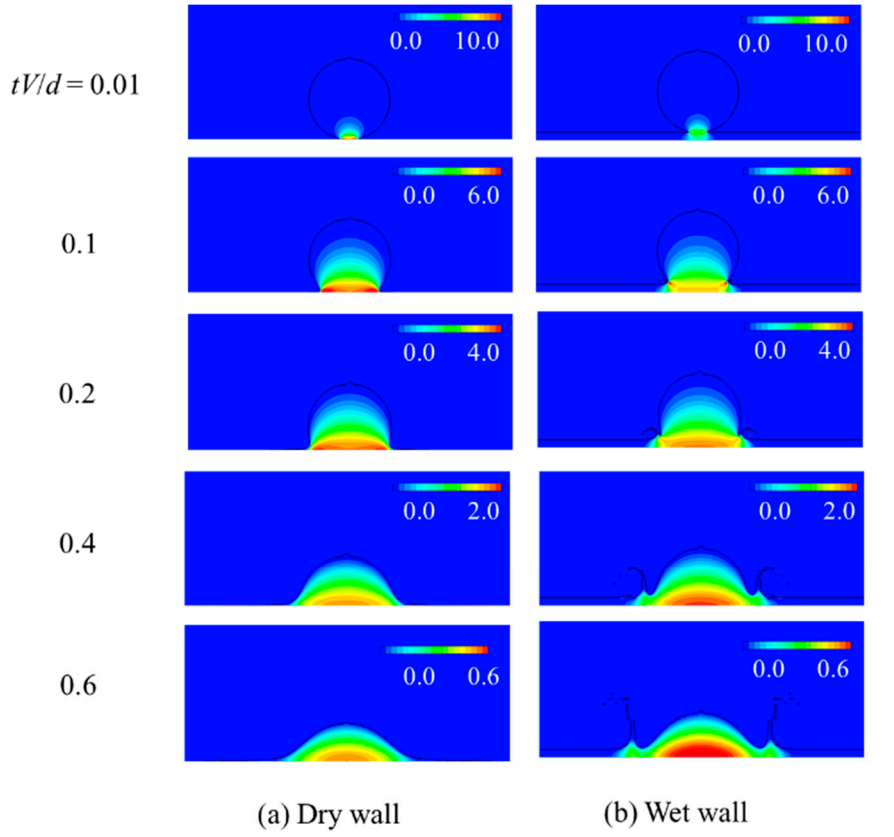


Figure 5. Time variation in the contours of the pressure coefficient C_p during droplet impact (V = 100 m/s).

3.2. Variation in Impact Pressure with Liquid-Film Thickness

Figure 6 shows the numerical results indicating the time variations in the central pressure coefficient C_{pc} on dry (h/d = 0) and wet walls with various liquid film thicknesses (h/d = 0.05, 0.1, 0.15, and 0.2). These results were obtained at an impact velocity of V = 100 m/s with a droplet diameter of d = 3 mm. The central pressure coefficient C_{pc} exhibited a peak immediately after the droplet impacted the wall, regardless of whether the wall was dry or wet. It subsequently decreased with increasing nondimensional time tV/d. However, the presence of the liquid film significantly reduced the central peak pressure coefficient C_{pcm}, resulting in a decreased pressure coefficient with increasing liquid film thickness. This indicates the impact pressure damping effect of the liquid film. Notably, the central peak pressure coefficient C_{pcm} is closely related to the initiation of erosion on the impacting wall. The numerical results indicated that the impact pressure was strongly correlated with the square of the impact velocity V^2 and was nearly independent of the impact velocity in the range of V = 50–150 m/s. The peak pressure coefficient at the central peak (C_{pcm} = 14) was observed on the drywall at a nondimensional time of tV/d = 0.01, whereas it shifted to a longer nondimensional time on the wet walls. Moreover, the central peak pressure on the wet wall was slightly higher than that on the drywall in the extended time range of tV/d = 0.2 to 1.2. This observation may indicate an increased impact force on the wet wall, as observed in the low-speed impact phenomenon of the droplet [34,37].

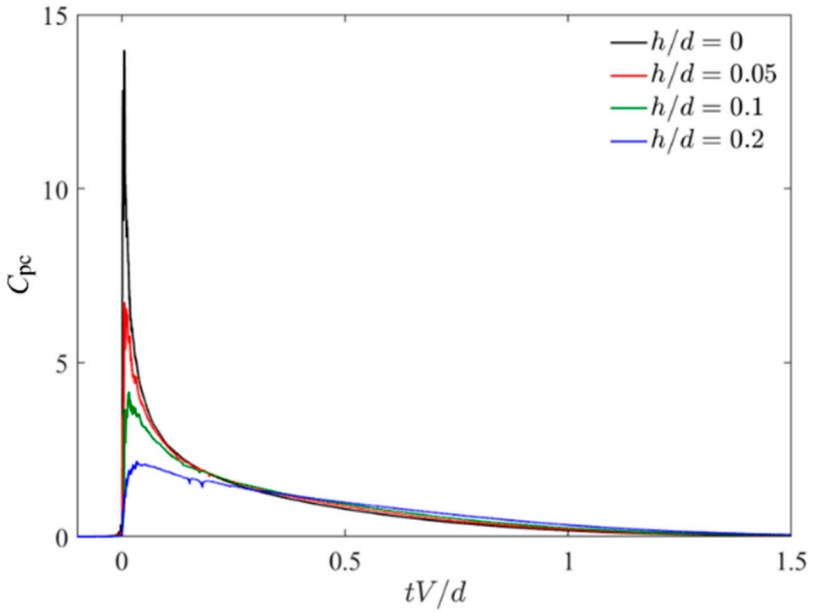


Figure 6. Time variation in the central pressure coefficient C_{pc} (V = 50 to 150 m/s).

Figure 7 illustrates the variation in the impact pressure ratio D_f (=p_w/p_d), which represents the ratio of the central peak pressure on the wet wall p_w to that on the drywall p_d. The results were plotted against the nondimensional liquid-film thickness h/d at an impact velocity of V = 100 m/s and a droplet diameter of d = 3 mm. These results are consistent with those of the impact velocities ranging from V = 50–150 m/s, indicating a minimal influence of impact velocity on the impact pressure ratio. This result can be attributed to the assumption of our numerical simulation of incompressible flow, which is reasonable considering that the impact velocity V = 100 m/s corresponds to a small Mach number of 0.07. The current numerical result was compared with that obtained from the compressible Navier–Stokes equation at V = 100 m/s [25]. Both results showed reasonable agreement with each other, suggesting the validity of the numerical results in the considered range of impact velocities, namely, from 50 to 150 m/s. The current numerical result can be ap-

proximated by a single line regardless of the impact velocity, which is represented by the following equation:

$$D_f = \exp\left\{a(h/d)^b\right\} \quad (6)$$

where the constants are determined as $a = -5.67$ and $b = 0.68$ through least square fitting in the velocity range of 50 to 150 m/s. This result indicates that the impact pressure ratio D_f decreases with increasing nondimensional liquid film thickness h/d, regardless of the impact velocity V. This indicates earlier erosion initiation for the thinner liquid film. Furthermore, the results show a sharp decrease in D_f as the liquid-film thickness increases, followed by a gradual decrease as the liquid-film thickness increases. This trend in the impact pressure ratio qualitatively agrees with that of earlier numerical findings for high-speed droplet impacts on a wet wall [25,27–30].

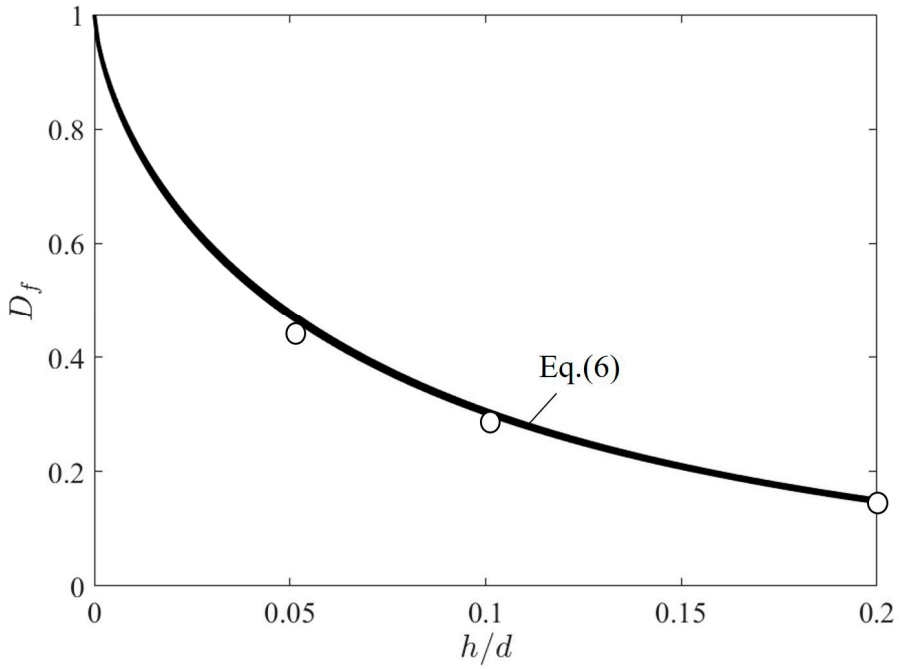


Figure 7. Variation in the impact pressure ratio D_f with liquid film thickness h/d (V = 50 to 150 m/s): ○ Fujisawa et al. [25] (V = 100 m/s).

3.3. Impact Pressure of the Droplet on the Rotating Blade

The nondimensional liquid-film thickness h/d on the rotating blade was determined using Equations (4) and (5) and the results are depicted in Figure 8 for impact velocities of V = 100 and 120 m/s, respectively, with a droplet diameter of d = 3 mm. The results are shown for three rainfall rates, namely, I = 2, 10, and 30 mm/h, corresponding to light, medium, and heavy [12], respectively. The blade radius ranges from R = 0.1 to 100 m, covering the short radius (R = 0.5 to 1.5 m) of the rain erosion tester and the long radius (R = 20 to 100 m) of the wind turbine. The results indicate that the nondimensional liquid-film thickness h/d increases with increasing radius R and rainfall rate I, whereas the film thickness slightly decreases with increasing impact velocity V. This suggests that the influence of the liquid film becomes small in high-speed flow applications [8]. The decrease in film thickness at high-impact velocities is attributed to the reduced viscous effect, whereas the influence of the liquid film cannot be disregarded in the low-impact velocity range relevant to wind turbine applications. We also found that the liquid-film thickness on the rain erosion tester (h/d = 0.005–0.01) was one order of magnitude thinner than that on the wind turbine blade (h/d = 0.05–0.1), regardless of the impact velocity. Therefore, the influence of the radial position on the film thickness is an important factor to consider, whereas the rainfall rate is also significant, particularly at longer radii.

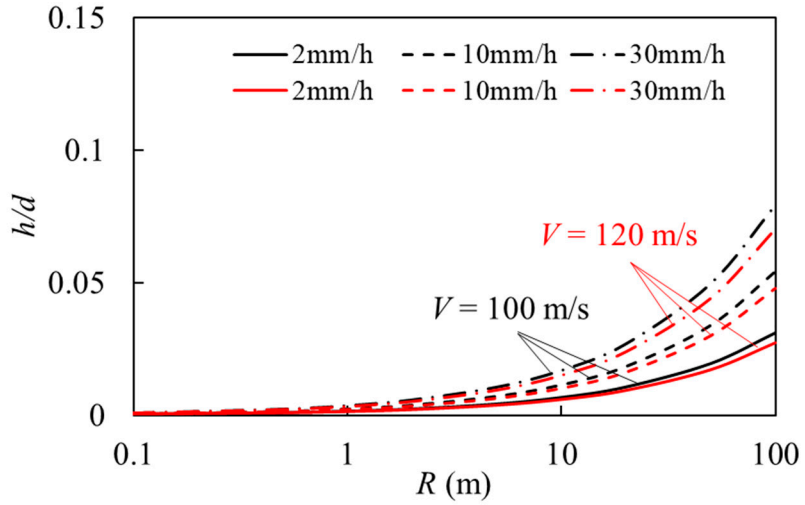


Figure 8. Radial variations in the nondimensional liquid film thickness h/d (d = 3 mm).

Figure 9 illustrates the radial variation in the impact pressure ratio D_f of the droplet impacting a wet wall of the rotating blade at impact velocities V = 100 and 120 m/s for three rainfall rates, namely, I = 2, 10, and 30 mm/h, with a droplet diameter d = 3 mm. The results were obtained from numerical simulations of the impact pressures of droplets on dry and wet walls using various combinations of radii R and rainfall rates I. We found that the impact pressure ratio D_f decreased with increasing radius R and rainfall rate I. Furthermore, the nondimensional impact pressure ratio of the wind turbine blade (R = 30 m) ranged from D_f = 0.56 to 0.73, which was lower than that of the rain erosion tester blade (R = 1 m), ranging from D_f = 0.88 to 0.94. Therefore, the impact pressure ratio is higher in the rain erosion tester blade than in the wind turbine blade, highlighting the significance of correcting the impact pressure ratio owing to varying liquid-film thicknesses. Notably, the impact pressure ratio increased slightly with increasing impact velocity; however, the variation was small compared with that owing to the effect of the radius. Furthermore, the nondimensional impact pressure ratio D_f decreased with increasing rainfall rate I owing to the increased liquid-film thickness.

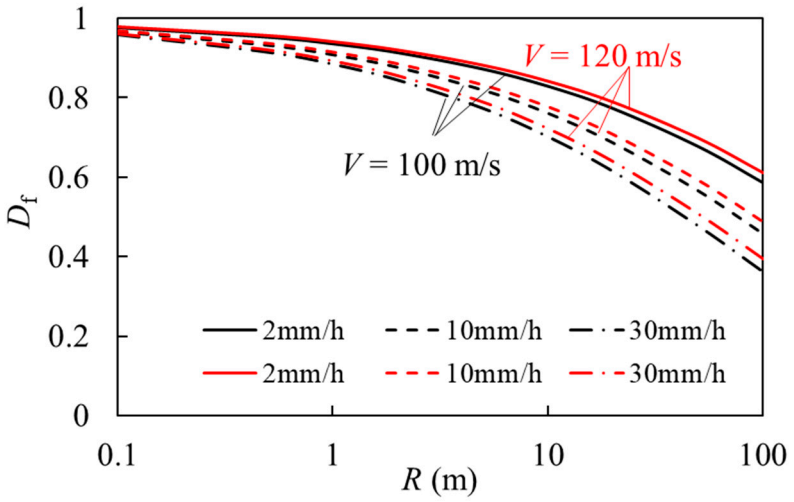


Figure 9. Radial variations in the impact pressure ratio D_f (=p_w/p_d) (d = 3 mm).

The V-N curve measured in the rain erosion tester can be used to predict the initiation of rain erosion on a wind turbine blade. However, the measured fatigue life may be influenced by the varying liquid-film thicknesses on the blades of the rain erosion tester and wind turbine. As the impact pressure is proportional to the squared impact velocity, the

impact pressure ratio can be converted into the impact velocity V_c, which is corrected for the effect of different liquid-film thicknesses. The corrected impact velocity V_c is defined by the following equation:

$$\frac{V_c}{V} = D_f{}^{\frac{1}{2}} \tag{7}$$

where V represents the impact velocity on the drywall.

Figure 10 illustrates the variations in the corrected impact velocity V_c normalized by the impact velocity V, plotted against the radius R of the blade for three rainfall rates I = 2, 10, and 30 mm/h. Our findings indicate that the velocity ratio V_c/V for the shorter radius is greater than that for the longer radius owing to the thinner liquid-film thickness on the rain erosion tester.

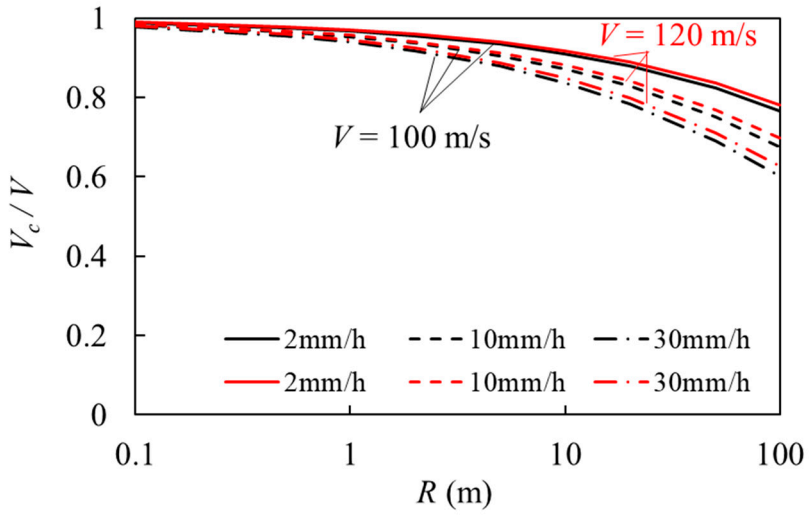


Figure 10. Radial variations in the corrected impact velocity V_c/V (d = 3 mm).

3.4. Estimation of the V-N Curve for a Wind Turbine Blade

Figures 11 and 12 show the flowchart and *V-N* curve, respectively, to estimate the fatigue life of the wind turbine blade based on the tests using the whirling arm rain erosion tester. When the impact velocity V, rainfall rate I, and droplet diameter d are given, the nondimensional liquid-film thickness h/d can be estimated using Equations (4) and (5) for the blades of the wind turbine and rain erosion tester. The impact pressure ratio D_f can then be estimated using Equation (6) for each wind turbine and rain erosion tester. This results in a corrected impact velocity V_c for each radius obtained from Equation (7). We assumed that the blade radii of the rain erosion tester and the wind turbine were R = 1 and 30 m, respectively, the rainfall rate I = 10 mm/h, and the impact velocity in the rain erosion tester V_1 = 100 m/s (subscript 1 denotes the rain erosion tester). The corrected impact velocity on the wind turbine blade can be evaluated as V_2 = 119.4 m/s from Equation (7) (subscript 2 denotes the corrected condition for the wind turbine blade); namely, 100 × 1.194 = 119.4 m/s. Here, the value 1.194 (=0.953/0.798) is the ratio of the rain erosion tester (R = 1 m, V_c/V = 0.953) to the wind turbine (R = 30 m, V_c/V = 0.798). Thus, the corrected *V-N* curve for the wind turbine blade can be represented by a broken line in Figure 12, which shows an impact velocity that is approximately 19% higher than that in the *V-N* curve of the rain erosion tester (solid line in Figure 12).

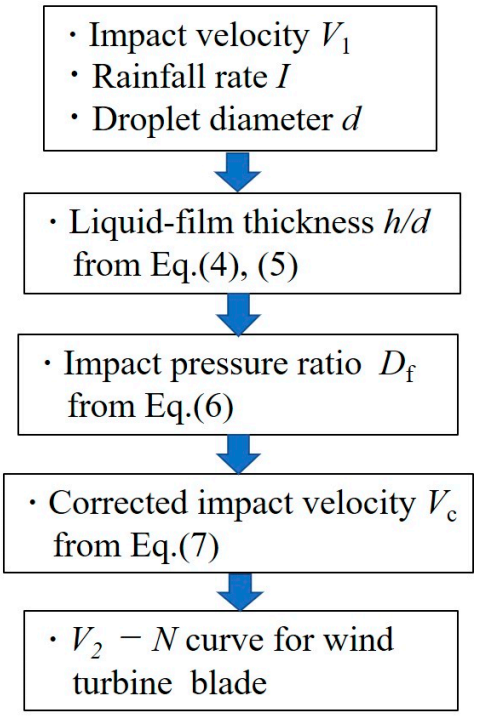


Figure 11. Flowchart for correcting the influence of liquid film thickness.

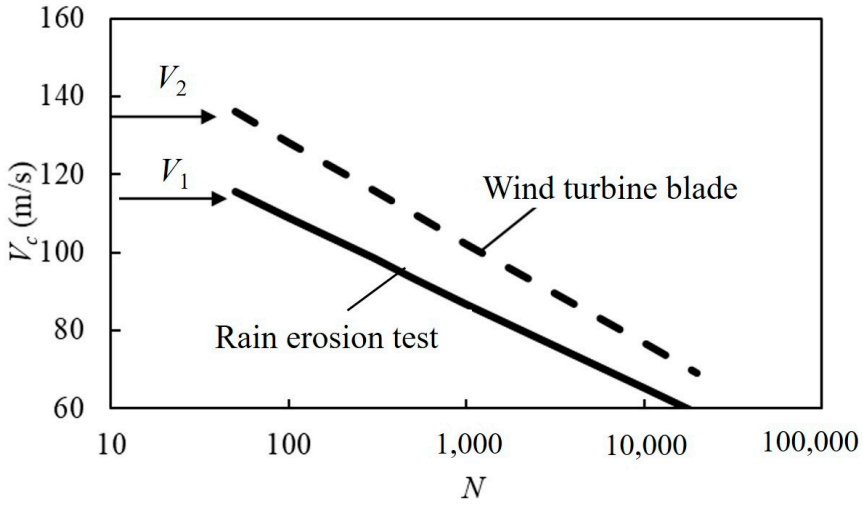


Figure 12. Example of *V-N* curve estimation for the wind turbine blade from the rain erosion tester.

4. Conclusions

To understand the influence of the liquid film on the impact pressure of a droplet on a wind turbine blade, a numerical simulation of liquid droplet impact on a wet wall was conducted by solving the incompressible form of the axisymmetric Navier–Stokes equation combined with an approximate solution of the liquid-film thickness on a rotating wall considering the centrifugal and Coriolis forces. Our results indicated that the impact pressure and droplet behavior were highly influenced by the liquid-film thickness; a thinner film thickness was observed on the shorter radius of the rain erosion tester caused by the increased centrifugal and Coriolis forces. Therefore, the peak impact pressure on the rain erosion tester blade increased more than that on the wind turbine blade owing to the thinner liquid film thicknesses. Based on these results, a correcting procedure for the impact pressure on the wind turbine blades was proposed by the rain erosion tester. This resulted

in an increased impact velocity for the *V-N* curve of the initiation of erosion compared with that obtained from the rain erosion tester.

Author Contributions: Conceptualization, N.F.; numerical simulation, N.F. and H.K.; visualization, N.F. and H.K., writing—original draft preparation, N.F.; writing—review and editing, N.F. and H.K. All authors have read and agreed to the published version of the manuscript.

Funding: This study was funded by the Fukushima Prefecture for the promotion of renewable energy.

Data Availability Statement: Data will be made available on request.

Acknowledgments: The authors acknowledge the support of M. Tanaka of the National Institute of Advanced Industrial Science and Technology (AIST).

Conflicts of Interest: The authors declare that there are no conflicts of interest that could be perceived as prejudicing the imparity of the research reported.

Nomenclature

C_p	pressure coefficient (=$(p - p_s)/(\frac{1}{2}\rho V^2)$) (-)
C_{pc}	central pressure coefficient (-)
C_{pcm}	central peak pressure coefficient (-)
D_f	impact pressure ratio (=p_w/p_d) (-)
d	droplet diameter (mm)
$\boldsymbol{F}$	external forces (-)
f	scalar function (-)
h	liquid-film thickness (mm)
I	rainfall rate (mm/h)
N	number of impacts (-)
p	pressure (Pa)
p_d	central pressure on drywall (Pa)
p_s	surrounding pressure (Pa)
p_w	central pressure on wet wall (Pa)
Q	volume flow rate (m^3/s)
R	radius of blade (m)
t	time (s)
V	impact velocity (m/s)
$\boldsymbol{V}$	velocity vector (-)
V_c	corrected impact velocity (m/s)
μ	viscosity of fluid (kg/(ms))
ν	kinematic viscosity of fluid (m^2/s).
ρ	density of fluid (kg/m^3)
ω	angular velocity of rotation (rad/s)
Subscript	
1	condition for the rain erosion tester
2	condition for the wind turbine blade

References

1. Heymann, F.J. Liquid Impingement Erosion. In *ASM Handbook*; ASM International: Tama, Japan, 1992; pp. 221–232.
2. Richman, R.H. Liquid-Impact Erosion, Failure Analysis and Prevention. In *ASM Handbook*; ASM International: Tama, Japan, 2002; pp. 1013–1018.
3. Fujisawa, N.; Morita, R. Liquid Droplet Impingement Erosion. In *ASM Handbook*; ASM International: Tama, Japan, 2021; pp. 764–772.
4. Mann, B.S.; Arya, V. HVOF coating and surface treatment for enhancing droplet erosion resistance of steam turbine blades. *Wear* **2003**, *254*, 652–667. [CrossRef]
5. Ahmad, M.; Schatz, M.; Casey, M.V. An empirical approach to predict droplet impact erosion in low-pressure stages of steam turbines. *Wear* **2018**, *402–403*, 57–63. [CrossRef]
6. Crockett, H.M.; Horowitz, J.S. Erosion in nuclear piping systems. *J. Press. Vessel Technol.* **2010**, *132*, 024501. [CrossRef]

7. Fujisawa, N.; Yamagata, T.; Hayashi, K.; Takano, T. Experiments on liquid droplet impingement erosion by high-speed spray. *Nucl. Eng. Des.* **2012**, *250*, 101–107. [CrossRef]
8. Gohardani, O. Impact of erosion testing aspects on current and future flight conditions. *Prog. Aero. Sci.* **2011**, *247*, 280–303. [CrossRef]
9. Dalili, N.; Edrisy, A.; Carriveau, R. A review of surface engineering issues critical to wind turbine performance. *Renew. Sustain. Energy Rev.* **2009**, *13*, 428–438. [CrossRef]
10. Keegan, M.H.; Nash, D.H.; Stack, M.M. On erosion issues associated with the leading edge of wind turbine blades. *J. Phys. D Appl. Phys.* **2013**, *46*, 383001. [CrossRef]
11. Slot, H.M.; Gelinck, E.R.M.; Rentrop, C.; Heidevan, E. Leading edge erosion of coated wind turbine blades: Review of coating life models. *Renew. Energy* **2015**, *80*, 837–848. [CrossRef]
12. Bartolomé, L.; Teuwen, J. Prospective challenges in the experimentation of the rain erosion on the leading edge of wind turbine blades. *Wind Energy* **2018**, *22*, 140–151. [CrossRef]
13. Eisenberg, D.; Laustsen, S.; Stege, J. Wind turbine blade coating leading edge rain erosion model, Development and validation. *Wind Energy* **2018**, *21*, 942–951. [CrossRef]
14. Herring, R.; Dyer, K.; Martin, F.; Ward, C. The increasing importance of leading-edge erosion and a review of existing protection solutions. *Renew. Sustain. Energy Rev.* **2019**, *115*, 109382. [CrossRef]
15. Ibrahim, M.E.; Medraj, M. Water droplet erosion of wind turbine blades: Mechanics, testing, modeling and future perspectives. *Materials* **2020**, *13*, 157. [CrossRef] [PubMed]
16. Fujisawa, N.; Johansen, N.F.-J.; Yamagata, T.; Fujisawa, K.; Tanaka, M. A review and comparative study of uncertainty in rain erosion testers for wind turbine blades. *J. Flow Energy* **2023**, *1*, 1–15.
17. *ASTM Standards G-73-10*; Standard Test Method for Liquid Impingement Erosion Using Rotating Apparatus. ASM International: Tama, Japan, 2017; pp. 294–312.
18. DNVGL. *Testing of Rotor Blade Erosion Protection Systems, Edition February, DNVGL-RP-0171*; DNVGL: Bærum, Norway, 2018; pp. 1–64.
19. R&DA/S Rain Erosion Tester. Available online: https://www.rd-as.com/rain-erosion-tester/ (accessed on 15 April 2021).
20. Bech, J.I.; Johansen, N.F.J.; Madsen, M.B.; Hannesdottir, A.; Hasager, C.B. Experimental study on the effect of drop size in rain erosion test and on lifetime prediction of wind turbine blades. *Renew. Energy* **2022**, *197*, 776–789. [CrossRef]
21. Brunton, J.H.; Rochester, M.C. Erosion of solid surfaces by the impact of liquid drops. *Treatise Mater. Sci. Technol.* **1979**, *16*, 186–248.
22. Tobin, E.F.; Young, T.M.; Raps, D.; Rohr, O. Comparison of liquid impingement results from whirling arm and water-jet rain erosion test facilities. *Wear* **2011**, *271*, 2625–2631. [CrossRef]
23. Zhang, S.; Johansen, K.D.; Bernad, P.L., Jr.; Kiil, S. Rain erosion of wind turbine blade coatings using discrete water jets: Effects of water cushioning, substrate geometry, impact distance, and coating properties. *Wear* **2015**, *328–329*, 140–148. [CrossRef]
24. Fujisawa, N.; Yamagata, T.; Saito, K.; Hayashi, K. The effect of liquid film on liquid droplet impingement erosion. *Nucl. Eng. Des.* **2013**, *265*, 909–917. [CrossRef]
25. Fujisawa, K.; Yamagata, T.; Fujisawa, N. Damping effect on impact pressure from liquid droplet impingement on wet wall. *Ann. Nucl. Energy* **2018**, *121*, 260–268. [CrossRef]
26. Haller, K.K.; Ventikos, Y.; Poulikakosa, D. Computational study of high-speed liquid droplet impact. *J. Appl. Phys.* **2002**, *92*, 2821–2828. [CrossRef]
27. Xiong, J.; Koshizuka, S.; Sakai, M. Investigation of droplet impingement onto wet walls based on simulation using particle method. *J. Nucl. Sci. Technol.* **2011**, *48*, 145–153. [CrossRef]
28. Sasaki, H.; Ochiai, N.; Iga, Y. Numerical analysis of damping effect of liquid film on material in high-speed liquid droplet impingement. *Int. J. Fluid Mach. Syst.* **2016**, *9*, 57–65. [CrossRef]
29. Sasaki, H.; Ochiai, N.; Iga, Y. Numerical study of high-speed liquid droplet impingement phenomenon by fluid/material coupled numerical method. *Jpn. J. Multiph. Flow* **2016**, *30*, 65–74. (In Japanese) [CrossRef]
30. Fujisawa, K.; Yamagata, T.; Fujisawa, N. Liquid droplet impingement erosion on groove roughness. *Nucl. Eng. Des.* **2018**, *330*, 368–376. [CrossRef]
31. Fujisawa, K.; Ohki, M.; Fujisawa, N. Influence of surface roughness on liquid droplet impingement erosion. *Wear* **2019**, *432–433*, 202955. [CrossRef]
32. Fujisawa, N. Liquid droplet impingement erosion on multiple grooves. *Wear* **2020**, *462*, 203513. [CrossRef]
33. Amirzadeh, B.; Louhghalam, A.; Raessi, M.; Tootkaboni, M. A computational framework for the analysis of rain-induced erosion in wind turbine blades, part I: Stochastic rain texture model and drop impact simulations. *J. Wind Eng. Ind. Aerody.* **2017**, *163*, 33–43. [CrossRef]
34. Fujisawa, N.; Kawabata, H.; Tanaka, M. Observing the impact force and low-speed droplet behavior of wet surfaces with very-thin liquid films. *Exp. Therm. Fluid Sci.* **2023**, *144*, 110836. [CrossRef]
35. Leshev, I.; Peev, G. Film flow on a horizontal rotating disk. *Chem. Eng. Process.* **2003**, *42*, 925–929. [CrossRef]

36. Fujisawa, N.; Aihara, A. Rain erosion mechanism on a leading-edge half cylinder. *Wear* **2023**, *532–533*, 205103. [CrossRef]
37. Yu, Y.; Hopkins, C. Experimental determination of forces applied by liquid water drops at high drop velocities impacting a glass plate with and without a shallow water layer using wavelet deconvolution. *Exp. Fluids* **2018**, *259*, 84. [CrossRef]

Disclaimer/Publisher's Note: The statements, opinions and data contained in all publications are solely those of the individual author(s) and contributor(s) and not of MDPI and/or the editor(s). MDPI and/or the editor(s) disclaim responsibility for any injury to people or property resulting from any ideas, methods, instructions or products referred to in the content.